Measurement of the high energy γ-rays from heavy ion reactions using Čerenkov detector*

Da-Wei Si [1,†] Yan Zhou,[1] Sheng Xiao,[1] Zhi Qin,[1] Dong Guo,[1] Yu-Hao Qin [1] Yi-Jie Wang,[1] Bo-Yuan Zhang,[1] Bai-Ting Tian,[1] and Zhi-Gang Xiao [1,‡]

[1]*Department of Physics, Tsinghua University, Beijing 100084, China*

The energetic bremsstrahlung photons up to 100 MeV produced in heavy ion collisions can be used as a sensitive probe for short-range correlation in atomic nuclei. The energy of the γ-rays can be measured by collecting the Čerenkov light in the medium induced by the fast electrons generated in the Compton scattering or electromagnetic shower of the incident γ ray. Two types of detectors based on pure water and lead glass as sensitive materials were designed for this purpose. The γ response and optical photon propagation in the detectors were simulated based on electromagnetic and optical processes in Geant4. The inherent energy resolutions of $0.022(4) + 0.51(2)/E_\gamma^{1/2}$ for water and $0.0026(3) + 0.446(3)/E_\gamma^{1/2}$ for lead glass were obtained. The geometry sizes of the lead glass and water were optimized to 30 cm$\times$ 30 cm$\times$ 30 cm and 60 cm$\times$ 60 cm$\times$ 120 cm, respectively, to detect high-energy γ-rays at 160 MeV. The Hough transform method was applied to reconstruct the direction of the incident γ-rays, providing the ability to experimentally distinguish the high-energy γ-rays produced in the reactions on the target from random background cosmic-ray muons.

Keywords: Bremsstrahlung γ-rays, Čerenkov, Geant4, Energy Resolution, Direction Reconstruction, Hough Transform

I. INTRODUCTION

Bremsstrahlung high-energy photons produced in heavy-ion reactions have attracted increasing interest because of their relevance to the nuclear equation of state (nEOS) and their short-range correlation in nuclei. In nEOS studies, particularly for nuclear matter with large neutron-to-proton asymmetry, a variety of isospin probes have been identified to constrain $E_{\rm sys}(\rho)$ (the density-dependent nuclear symmetry energy), including the preequilibrium n/p yield ratio [1], n/p differential flow [2, 3] and bremsstrahlung high-energy photons [4]. Among these probes, bremsstrahlung γ-rays created by heavy ion collisions are clearly observable because of their rare interactions with the medium after they are produced. Very recently, it has been revealed that bremsstrahlung high-energy γ-rays carry information on the high-momentum tail (HMT) of nucleons, giving rise to the short-range correlation effect in nuclei [5–8]. On the other hand, however, the experimental data in this direction is quite scarce.

Recently, the full γ energy spectrum up to 80 MeV was measured in reactions ^{86}Kr+^{124}Sn at 25 MeV/u with a 15-unit CsI(Tl) hodoscope mounted on a compact spectrometer for heavy-ion experiments (CSHINE) [9–13]. It has been demonstrated that the γ energy spectrum above 20 MeV is reproduced fairly well by transport model simulations that incorporate γ production from incoherent np scattering with an approximate 15% HMT ratio [14]. However, CsI(Tl) is a slow detector, and the microsecond response time of CsI(Tl) crystals makes it difficult to reconstruct the total energy from multiple firing units. Therefore, we are motivated to develop a fast and relatively cheap detector containing a sufficiently large-volume-sensitive material to detect high-energy γrays in heavy-ion reactions. The Čerenkov radiation [15] detector is a favorable option because of its fast response time in the order of tens of nanoseconds and its ability to infer the incident direction information of the initial γ-rays, the latter of which can be used to suppress the cosmic-ray muon background from random directions.

In this paper, we report the design of a Čerenkov γ calorimeter using water and lead glass as sensitive media. Based on Geant4 packages, the geometric size of the detectors was optimized. The energy resolution was obtained by tracking each Čerenkov photon before it arrived at the photomultiplier tube (PMT) for which the quantum response was modeled. The incident direction reconstruction was implemented using the Hough transform method. The remainder of this paper is organized as follows. Section II describes the simulations framework of the calorimeter. Section III presents the optimization of the detector size and the reconstruction of γ direction. Finally, Sect. IV concludes the paper.

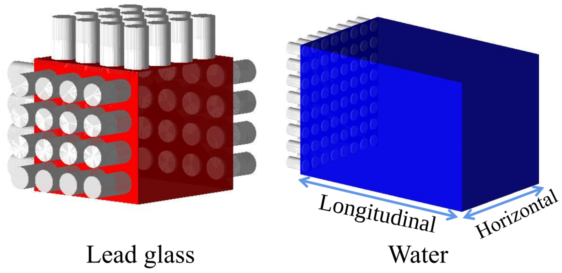

Fig. 1. (Color online) Detector configuration with two sensitive volumes, lead glass (left) and pure water (right), respectively.

* This work was supported by the Ministry of Science and Technology (2020YFE0202001), by the National Natural Science Foundation of China (Nos. 11961141004 and 12205160), and Tsinghua University Initiative Scientific Research Program.

† Corresponding author: sdw21@mails.tsinghua.edu.cn
‡ Corresponding author, xiaozg@tsinghua.edu.cn

II. SIMULATION SETUP

In this study, Geant4 (version 4.10.05)[16] packages were used for Monte Carlo simulation and optimization of the detector. "QBBC" and "G4OpticalPhysics" are applied as the physical process list to describe the electromagnetic (EM) showers of γ rays in materials, and to model the generation and transport of Čerenkov photons. For each event in the simulations, incident γ-rays hit the front of the detector. Then, Čerenkov photons are generated if fast electrons are produced by Compton scattering or e^-e^+ generation. Each Čerenkov photon is tracked to its termination, either to be absorbed during propagation or to reach the surface of the PMTs, where the waveform pulse of the given parameters is generated with a certain quantum efficiency. The waveforms were recorded at intervals of 2 ns for digitization. The final data corresponding to each incident γ ray are saved as a matrix of $N_1 \times N_2$ dimensions, where N_1 represents the number of fired PMTs and N_2 represents the number of sampling points for the corresponding waveform.

A. Detector geometry

The detector structure and locations of the PMTs are shown in Fig. 1 for lead glass and water as sensitive materials, defined as "G4_GLASS_LEAD"(left) and "G4_WATER"(right), respectively. The water tank size was 60 cm×60 cm×120 cm, and the size of the lead glass was 30 cm×30 cm×30 cm. The PMTs were arranged in an 8×8 array with a water configuration. In the lead glass configuration, the PMTs were arranged in 4×4 arrays on the four sides of the detecting tank. The diameter of each PMT was 51 mm, and the distance between each neighboring PMT pair was 70 mm, both vertically and horizontally.

B. Optical process

Upon invoking the Čerenkov mechanism in Geant4, the energy and number of Čerenkov photons were sampled in each G4step according to[17].

$$\frac{\mathrm{d}^2 N}{\mathrm{d}\lambda \mathrm{d}L} = \frac{2\pi\alpha Z^2}{\lambda^2} \sin^2\theta_{\mathrm{c}} \tag{1}$$

where θ_c is the Čerenkov angle, λ is the wavelength of the Čerenkov photon. The initial position of Čerenkov photons is uniformly distributed in every G4step, the emission angle is calculated according to the refractive index of materials and the speed of the charged particle, the outgoing azimuth is uniformly distributed within the range of 2π, we set a maximum of 100 photons emitted in each step to ensure the detailed sampling. In the process of photon transport, the transmission characteristics of photons in a material and their behavior at the boundary between the two materials must be defined. In this simulation, we defined the scattering and absorption lengths between the Čerenkov photons and water molecules by referring to the test data of IceCube [18, 19]. Owing to the lack of optical parameters for lead glass, we conservatively defined an attenuation efficiency of 70% for a 10 cm propagation. For the boundary characteristics [20, 21], we used UNIFIED model [22, 23] in Geant4 and selected "dielectric-dielectric" option to describe the interface between the material and PMTs. In this model, Geant4 determines the photon boundary behavior according to the Fresnel formula and the refractive index on both sides. For the remaining boundaries, we use the dielectric_LUT model [24] and select a polished Teflon_LUT boundary. Thus, Geant4 determines the reflection, refraction, and absorption of photons based on the built-in parameters.

C. PMT Response

In the full case, photons are converted into photoelectrons with a certain quantum efficiency after hitting the PMT, and a pulse is formed after multiplication. A pulse formed by a single photon is described in [25]

$$V_{\mathrm{pulse}}(t) = \begin{cases} G\exp(-\frac{1}{2}(\frac{t-t_{\mathrm{i}}}{\sigma} + e^{-\frac{t-t_{\mathrm{i}}}{\sigma}})), & t \leq t_{\mathrm{i}} \\ G\exp(-\frac{1}{2}((\frac{t-t_{\mathrm{i}}}{\sigma})^{0.85} + e^{-\frac{t-t_{\mathrm{i}}}{\sigma}}), & t > t_{\mathrm{i}} \end{cases} \tag{2}$$

where $t_{\mathrm{i}} = t_{\mathrm{hit}} + t_{\mathrm{trans}}$ and t_{hit} represent the time at which a photon hits the PMT, $t_{\mathrm{trans}} = 29$ ns represents the electron transit time of the PMT, $\sigma = 1.2$ ns represents the transit time spread. The final waveform is generated by superimposing all single-photon waveforms when multiple photons are converted into photoelectrons, as shown in Fig. 2 (a). Based on the incidence of γ rays, the waveform of each PMT within 240 ns was recorded as the final data. Figure 2(b) shows the distribution of the time at which the optical photons reach the PMTs in the lead-glass configuration, which was extracted by linearly fitting the rising edge of the waveform [26]. This illustrates that most photons reach the surface of PMTs between 26 ns and 31 ns after γ emission, which means that we can distinguish between direct and scattered photons according to the distribution in the direction reconstruction (see Sect. III).

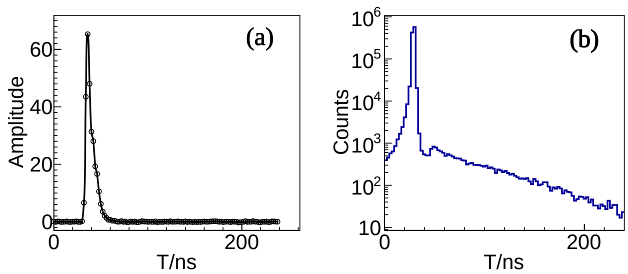

Fig. 2. (Color online) (a) a typical waveform for PMT, (b) the distribution of the time when optical photons reach PMTs in lead glass detector.

III. RESULT AND DISCUSSION

A. Influence of detector size on energy resolution

We used the photoelectron peak number $\langle n_{\rm pe}\rangle$ and the energy resolution, defined by $\delta_{E_\gamma} = \delta_{n_{\rm pe}} = \sigma_{n_{\rm pe}}/\langle n_{\rm pe}\rangle$, to optimize the detector design. In the simulation, such high-energy γ rays hit the center of the front surface of the detector perpendicularly. The shower electrons and positrons, if produced with a velocity exceeding the speed of light in the medium, will generate Čerenkov light propagating to the PMT, where the photoelectrons are generated. Owing to the statistical fluctuations, the number of photoelectrons varies. Figure 3 (a) presents the distribution of the number of photoelectrons for 50 MeV incident γ-ray in the lead-glass detector as an example. In the following analysis, the photoelectron peak number $\langle n_{\rm pe}\rangle$ was considered as the average number of photoelectrons. Figure 3 (b) presents the distribution of $\langle n_{\rm pe}\rangle$ as a function of incident γ energy E_γ for the two configurations at their own optimized volumes (see below). For a detector of a given size, $\langle n_{\rm pe}\rangle$ has a linear dependence on E_γ. Thus, the γ-ray energy can be measured using the number of photoelectrons.

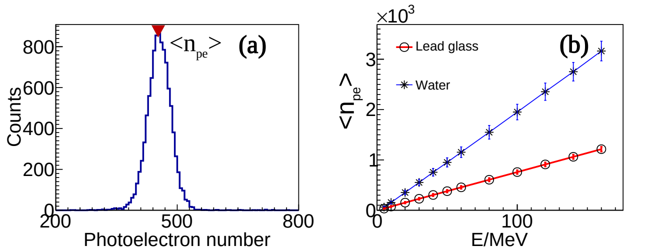

Fig. 3. (Color online) (a)the spectrum of the photoelectron yield for 50 MeV γ rays in lead glass detector,(b) Linear response of the calorimeter.

We then optimized the detector size at a given maximum γ energy of 160 MeV, which covered the range of interest for E_γ in heavy-ion reactions at Fermi energies. For each event, the distribution of photoelectron number was analyzed to obtain $\langle n_{\rm pe}\rangle$ and its standard deviation ($\sigma_{n_{\rm pe}}$). If the detector medium is too small, much of the γ-ray energy will leak outside the sensitive volume. However, if the detector medium is too large, Čerenkov photons are scattered many times and gradually absorbed, leading to a reduction in the number of photoelectron collected by PMTs. These two factors collectively determine the energy resolution. Figure 4(a) and (c) illustrate the energy resolutions δ_{E_γ} and $\langle n_{\rm pe}\rangle$ as functions of the horizontal and longitudinal lengths of the lead-glass configuration. Clearly, as the horizontal and longitudinal lengths increased, δ_{E_γ} reaches its lowest point at 30 cm, whereas $\langle n_{\rm pe}\rangle$ decreases when the horizontal or longitudinal lengths exceed 30 cm. Thus, 30 cm$\times$ 30 cm$\times$ 30 cm is the optimal size of the lead glass. Figure 4(b)(d) show the same quantities for the pure water configuration. As the longitudinal length increases, the energy resolution δ_{E_γ} decreases gradually and converges to 6%, and $\langle n_{\rm pe}\rangle$ first increases and then decreases because Čerenkov light attenuation becomes the main factor after the longitudinal length exceeds 80 cm. As the horizontal length increases, δ_{E_γ} reaches its minimum at 60 cm, beyond which $\langle n_{\rm pe}\rangle$ starts to decrease. Thus, 60 cm $\times$ 60 cm $\times$ 120 cm was the optimal size for water.

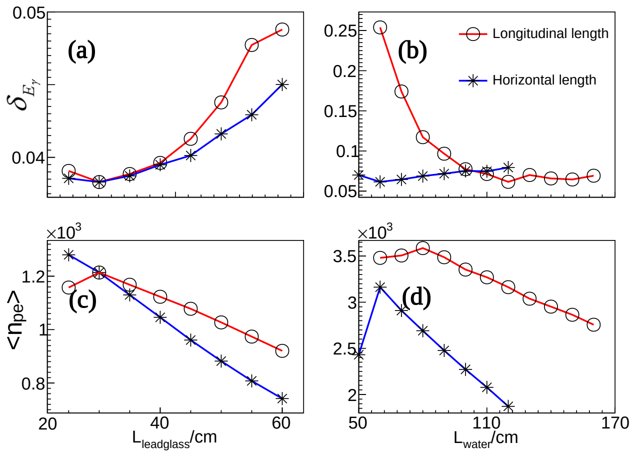

Fig. 4. (Color online) process of size optimization.(a)relationship between energy resolution and detector size for lead glass, (b)relationship between energy resolution and detector size for water, (c) relationship between $\langle n_{\rm pe}\rangle$ and detector size for lead glass, (d)relationship between $\langle n_{\rm pe}\rangle$ and detector size for water.

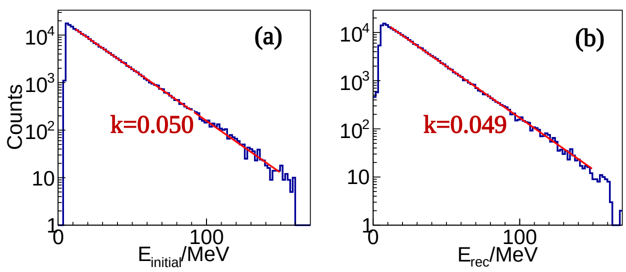

Fig. 5. (Color online) The initial(a) and reconstructed(b) γ energy spectra in lead glass configuration.

Given the good linear response of the water and lead glass Čerenkov calorimeter to the γ energy, as shown in Fig. 3 (b), one can reconstruct the γ energy from the signal height equivalent to the number of photoelectrons. To test this ability, we simulated the detector response for 10^5 γ events with an initial energy $E_{\rm initial}$ in an exponential distribution. The slope of the input exponential distribution is set to -0.05, as shown in Fig. 5 (a). The reconstructed energy ($E_{\rm rec}$) is plotted in panel (b) with the slope parameter fitted at -0.049. It is shown that the Čerenkov calorimeter of lead glass measures high-energy γ in the range from 5MeV to 160MeV. Figure 6 shows the resolution at various incident energies for the lead glass and water configurations. Inherent resolutions of $0.022(4) + 0.51(2)/E_\gamma^{1/2}$ for water and $0.0026(3) + 0.446(3)/E_\gamma^{1/2}$ for lead glass were obtained by fitting the simulated data points. At high energies(above 100

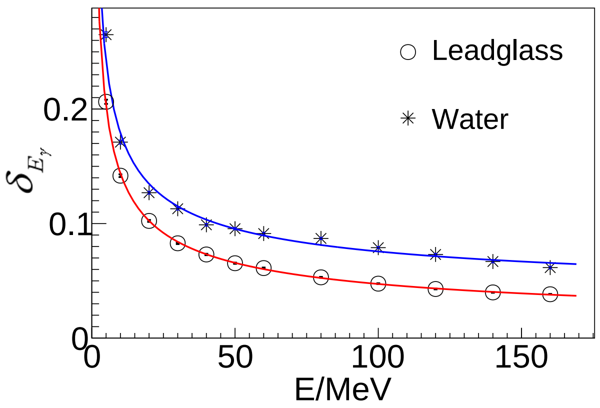

Fig. 6. (Color online) Resolution prediction of the calorimeter of water and lead glass, respectively.

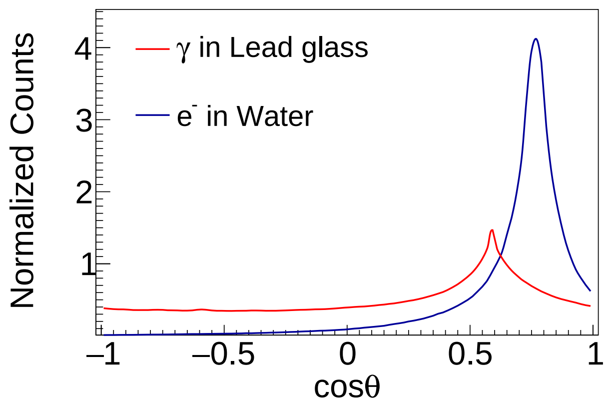

Fig. 7. (Color online) Čerenkov photon direction distribution for electron incidence in water and γ ray incidence in lead glass, respectively.

MeV), the resolutions were saturated at approximately 7.3% and 4.7%.

B. Direction reconstruction

It is well known that a definite angle exists between the Čerenkov photons and charged particles [17], which is the basis for direction reconstruction. In fact, γ shower also partially retains this feature. Figure 7 shows the angle distribution between the Čerenkov radiation direction and the initial direction of electrons (γ rays) in water (lead glass), which was obtained by the Geant4 simulation, where the energies of electrons and γ were sampled evenly from 5 to 160 MeV in the simulation. The refractive index of lead glass and water are 1.7 and 1.3, so the cosine of their Čerenkov angle are $\cos\theta_c \approx 0.58$ and 0.77, respectively. According to Fig. 7, although the e^+e^- pair production and Compton effect may cause scattering, the emission angle distribution of the Čerenkov photons produced by the EM shower is still related to the initial direction of γ rays. This suggests that the direction of γ rays can be reconstructed by referring to the electron direction reconstruction method used in large experiments, such as the Super-Kamiokande and Sudbury Neutrino Observatory(SNO) [28, 29]. It was found in our work that the Čerenkov photons experience scattering many times before reaching PMTs in water because of the overlength of the medium, heavily smearing the initial direction information; therefore, we only reconstructed the γ ray direction in the lead glass configuration.

1. Vertex reconstruction

To reconstruct the direction of the electrons, it is usually assumed that the electrons emit Čerenkov light from a fixed point. According to the angle distribution in Fig. 7, it can be assumed that the γ rays emit Čerenkov light from a fixed point with a specific Čerenkov angle; hence, the time taken for photons to reach the PMT can be expressed as [30, 31]

$$t_{\rm hit} = \frac{|\vec{X}_{\rm pmt} - \vec{X}_{\rm vtx}|}{v} + t_0 \tag{3}$$

where t_0 represents the moment when the Čerenkov light is generated, $t_{\rm hit}$ represents the moment when the photon hits PMTs, v is the velocity of light in lead glass, $\vec{X}_{\rm pmt}$ and $\vec{X}_{\rm vtx}$ are the coordinate of the PMT and the vertex respectively. In our analysis, the optimal estimation of the vertex coordinates is obtained by minimizing the χ^2 of fitting the time distribution with formula (3), in which the t_0 and $\vec{X}_{\rm vtx}$ are fitting parameters. For each γ event, the timing of each PMT was extracted by linear fitting to the rising edge of the waveform, where the crossing point of the linear fitting and the zero baseline was taken as the timing signal of the PMTs [26]. The spatial coordinates of each firing PMT are used as $\vec{X}_{\rm pmt}$. Because the reflector layer is set in the simulation, some Čerenkov photons are reflected before hitting the PMTs and the timing signals deviate from (3). So according to Fig. 2(b), we only selected the PMTs with the hit time being less than 1.5 ns before the peak and 1 ns after the peak of the time distribution. We define the coordinates of the center of the lead glass as $(0\,\rm cm, 0\,\rm cm, 0\,\rm cm)$. Figure 8 shows the χ^2 distribution of the vertex coordinate fitting for a 10 MeV γ-ray incidence, indicating the optimal vertex coordinate at $(1.29\,\rm cm, -1.11\,\rm cm, -6.34\,\rm cm)$.

2. Hough transform

The Hough transform [32–34] has been successfully applied to identify Čerenkov rings that can map the vector space of the vertex-to-PMT direction to that of the electron incident direction. An example of this application is SuperKamiokande [35]. Similarly, we can define the vector

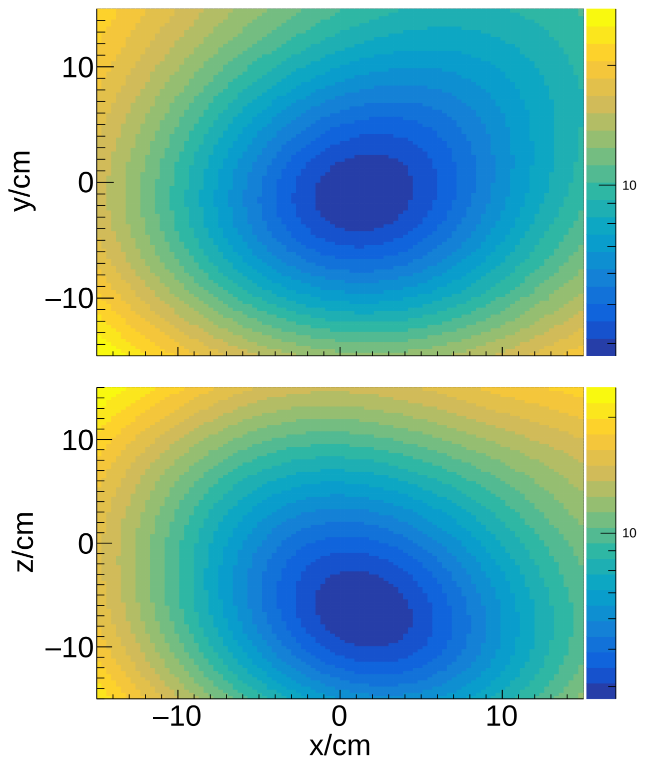

Fig. 8. (Color online) The χ^2 distribution contour in the coordinate space of the vertex fitting.

from the vertex of the γ ray to the firing PMT and the initial direction vector of the γ ray as $\vec{V}_{\rm p}$ and $\vec{V}_{\gamma}$ respectively, where θ represents the angle between the two vectors. The probability distribution of θ is indicated by the red line in Fig. 7. The vector space of the incident direction of γ-ray was divided by 100×100 according to ($\cos\theta$,ϕ), and the weight of each cell can be expressed as

$$W_{\rm ij} = \sum_{1}^{k} f(\cos\theta_{\rm ijk}), \quad \cos\theta_{\rm ijk} = \vec{V}_{\gamma \rm ij} \cdot \vec{V}_{\rm pk} \tag{4}$$

$\vec{V}_{\gamma \rm ij}$ represents the central unit vector of the cell at row i and column j in the vector space of incident direction of γ ray, $\vec{V}_{\rm pk}$ represents the unit vector from the vertex pointing to the center of $k^{\rm th}$ firing PMT, and function f represents the Čerenkov angle distribution function of γ rays (the red line in Fig 7) in lead glass. Figure 9 shows the event display of Hough transform for an incident γ event in the direction $(0.068, 0.063, -0.995)$. Figure 9(a) shows the hit PMTS position distribution for this event, where the color represents the signal amplitude in the corresponding PMT. Figure 9(b) shows the result of the Hough transform for the $1^{\rm st}$ PMT, Fig 9(c) shows the cumulative result of the Hough transform for all firing PMTs, and the brightest point in Fig. 9(c) represents the optimal estimate of the incident gamma direction. For example, the optimal estimates

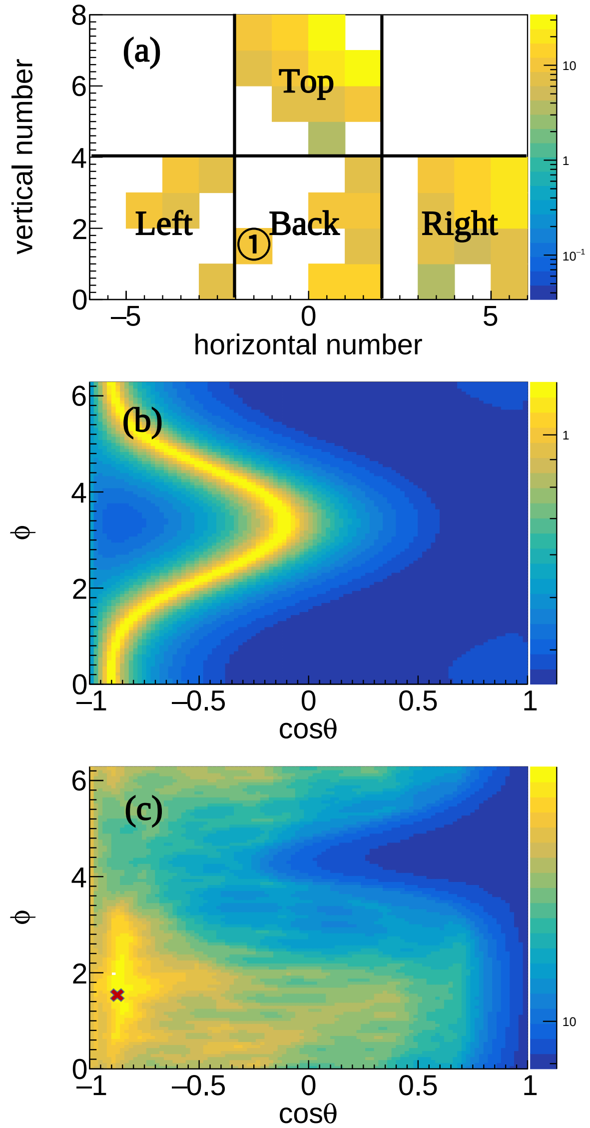

Fig. 9. (Color online) Event display of Hough transformation. (a) is the position distribution of firing PMTs, there are four sides to place PMTs in lead glass configuration, top, left, right, and back, (b) is the result of Hough transform for the marked $1^{\rm st}$ PMT on the back surface, (c) is the cumulative result of Hough transform for all firing PMTs in the time window. The cross indicates the optimized direction.

are $(-0.077^{+0.12}_{-0.15}, 0.487^{+0.08}_{-0.08}, -0.87^{+0.05}_{-0.03})$, and the deviation from the initial incidence direction is $26.9^{+3.5}_{-4.4}{}^{\circ}$ for this event.

Figure 10 shows the distribution of $\cos\Delta\theta$, where $\Delta\theta$ is the angle between the reconstructed direction and the initial direction of γ-rays hitting the front of the lead glass uniformly from the target. The peak of the cosine values is close to $\cos\Delta\theta = 1$, indicating that the detector can reconstruct the direction of the signal in the lead-glass configuration. However, the cosine distribution broadens considerably because of the rough assumption that γ rays emit Čerenkov light at a

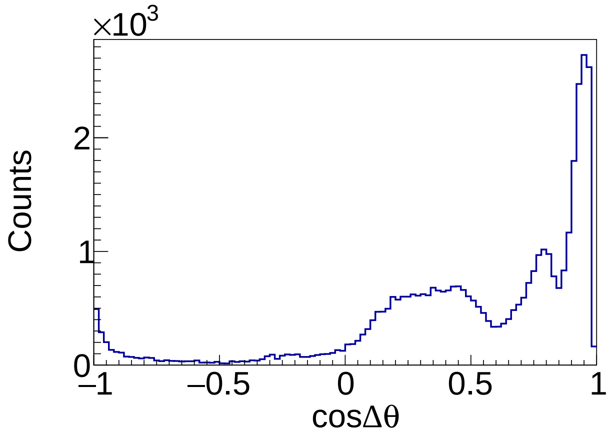

Fig. 10. (Color online) The distribution of the angle between initial and reconstructed direction of γ rays

fixed point. In fact, according to the red line in Fig. 7, most γ rays would generate Čerenkov light in a path whose length is comparable to the detector size, which contributes to the bias in the direction reconstruction. The antisymmetry of the locations of the PMTs also causes bias.

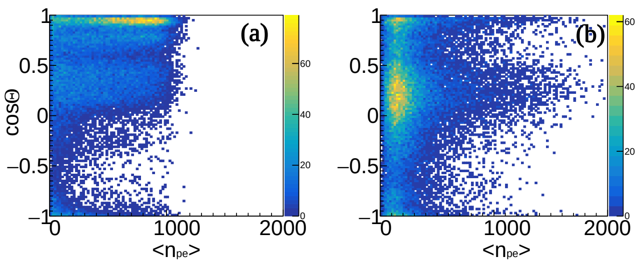

Fig. 11. (Color online) Two-dimensional distribution of $\cos\Theta$ and $\langle n_{\rm pe}\rangle$ for γ rays(a) from the reaction target and for cosmic ray muons (b).

3. *Discrimination between γ and cosmic ray muon*

In a real beam experiment, only γ rays from the reactions on the target are of interest. Because the direction of γ rays from the reaction target is different from that of the cosmic rays, it provides a way to suppress the background. To test the ability to suppress the cosmic-ray background, we generated γ rays with energies between $5-160$ MeV at the front of the detector and mixed them with uniform μ^- emissions from the top of the detector. The μ^- energy E_μ (in GeV) and zenith angle θ_μ were sampled using the Gaisser formula [36]

$$\frac{\mathrm{d}I}{\mathrm{d}E_\mu \mathrm{d}\cos\theta_\mu} = \frac{0.14}{E_\mu^{2.7}}\left[\frac{1}{1+\frac{1.1E_\mu\cos\theta_\mu}{115}} + \frac{0.054}{1+\frac{1.1E_\mu\cos\theta_\mu}{850}}\right] \tag{5}$$

Considering that the threshold for μ^- to produce Čerenkov radiation in lead glass was 78 MeV, we set the sampling range to $80-1000$ MeV. The physical quantity Θ denotes the angle between the reconstructed direction and vector from the reaction target to the fitted vertex vector. Figure 11 shows the two-dimensional distributions of cosΘ and $\langle n_{\rm pe}\rangle$ for γ rays from the target (a) and cosmic rays (b), respectively. A very different feature between the reaction γ rays and the cosmic-ray muon background is evident. The $\cos\Theta$ of γ rays is concentrated above 0.5, $\langle n_{\rm pe}\rangle$ is relatively evenly distributed between 0 and 1000, whereas the cosΘ of μ^- is concentrated between 0 and 0.5, and $\langle n_{\rm pe}\rangle$ is concentrated around 200. Therefore, the directivity of the Čerenkov light provides new dimensional information to distinguish the signal from the background.

IV. CONCLUSION

In this study, we investigated the feasibility of using a Čerenkov calorimeter to detect bremsstrahlung γ rays from heavy-ion reactions at Fermi energies. A full framework was established to simulate the response and performance of the Čerenkov gamma calorimeter based on Geant4 packages, including γ-induced EM shower, Čerenkov photon generation and propagation, and the parameterization of PMT waveform. The optimal volume, linear response, and energy resolution of the detector were obtained using water and lead glass as sensitive media. The inherent energy resolutions at $0.022(4) + 0.51(2)/E_\gamma^{1/2}$ level for water and $0.0026(3)+0.446(3)/E_\gamma^{1/2}$ level for lead glass were predicted. It was demonstrated that the initial direction of γ rays can be reconstructed using the vertex fit and Hough transform method, showing the ability to distinguish the bremsstrahlung γ rays produced in the reactions from the cosmic-ray muon background in a real beam experiment. The detector is built and applied briefly to measure the high-energy γ rays produced in heavy-ion reactions.

[1] M. A. Famiano, T. Liu, W. G. Lynch et al., Neutron and Proton Transverse Emission Ratio Measurements and the Density Dependence of the Asymmetry Term of the Nuclear Equation of State.Phys. Rev. Lett **97**, 052701 (2006). doi: 10.1103/PhysRevLett.97.052701

[2] Y.J. Wang, C.C Guo, Q.F. Li et al., 3H/3He ratio as a probe of the nuclear symmetry energy at sub-saturation densities. Eur. Phys. J. A **51**, 37 (2015). doi: 10.1140/epja/i2015-15037-8

[3] Y.J. Wang, Q.F. Li, Application of microscopic transport model in the study of nuclear equation of state from heavy ion collisions at intermediate energies. Front. Phys. **15**, 44302 (2020). doi: 10.1007/s11467-020-0964-6

[4] G.C. Yong, B.A. Li, L.W. Chen, Neutron–proton bremsstrahlung from intermediate energy heavy-ion reac-

tions as a probe of the nuclear symmetry energy. Phys. Lett. B **661**, 82(2008) doi: 10.1016/j.physletb.2008.02.013

[5] W. Bauer, G.F. Bertsch, W. Cassing et al., Energetic photons from interiiiediate energy proton- and heavy-ion-induced reactions. Phys. Rev. C **34**, 2127(1986) doi: 10.1103/PhysRevC.34.2127

[6] H. Xue, C. Xu, G.C. Yong et al., Neutron–proton bremsstrahlung as a possible probe of high-momentum component in nucleon momentum distribution. Phys. Lett. B **755**, 486(2016) doi: 10.1016/j.physletb.2016.02.044

[7] A.N. Antonov, V.A. Nikolaev, I.Zh. Petkov, Nucleon momentum and density distributions of nuclei. Z Physik A **297**, 257(1980). doi: 10.1007/BF01892806

[8] W.M. Guo, B.A. Li, G.C. Yong, Imprints of high-momentum nucleons in nuclei on hard photons from heavy-ion collisions near the Fermi energy. Phys. Rev. C **104**, 034603(2021) doi: 10.1103/PhysRevC.104.034603

[9] F.H. Guan, X.Y. Diao, Y.J. Wang et al., A compact spectrometer for heavy ion experiments in the Fermi energy regime. Nucl. Inst. Meth. A **1011**, 165592 (2021). doi: 10.1016/j.nima.2021.165592

[10] F.H. Guan, Y.J. Wang, X.Y. Diao et al., Track recognition for the telescopes with silicon strip detectors. Nucl. Inst. Meth. A **1029**, 166461 (2022) doi: 10.1016/j.nima.2022.166461

[11] Y.H. Qin, D. Guo, S. Xiao et al., A CsI(Tl) hodoscope on CSHINE for Bremsstrahlung γ-rays in heavy ion reactions. Nucl. Inst. Meth. A **1053**, 168330 (2022) doi: 10.1016/j.nima.2023.168330

[12] D. Guo, Y.H. Qin, S. Xiao et al., An FPGA-based trigger system for CSHINE. Nucl. Sci. Tech. **33**, 162(2022) doi: 10.1007/s41365-022-01149-0

[13] Y.J. Wang, F.H. Guan, X.Y. Diao et al., CSHINE for studies of HBT correlation in Heavy Ion Reactions. Nucl. Sci. Tech. **32**, 4(2021) doi: 10.1007/s41365-020-00842-2

[14] Y.H. Qin, Q.L. Niu, D. Guo et al., Probing high-momentum component in nucleon momentum distribution by neutron-proton bremsstrahlung γ-rays in heavy ion reactions. arXiv:2307.10717v1 doi: 10.48550/arXiv.2307.10717

[15] Z.H. Fan, J.C. Liang, H.R. Liu et al., Influence of wall effect on detection efficiency of β-emitters in TDCR-Čerenkov method. NUCLEAR TECHNIQUES **46**, 6(2023) doi: 10.11889/j.0253-3219.2023.hjs.46.060504

[16] S. Agostinelli, J. Allison, K. Amako et al., Geant4–a simulation toolkit. Nucl. Inst. Meth. A **506**, 250(2022). doi: 10.1016/S0168-9002(03)01368-8

[17] I.M. Frank, I.E. Tamm, Coherent visible radiation of fast electrons passing through matter. Compt. Rend. Acad. Sci. URSS. **14**, 109(1937). doi: 10.3367/UFNr.0093.196710o.0388

[18] J. Lundberg, P. Miočinović, K. Woschnagg et al., Light tracking through ice and water—Scattering and absorption in heterogeneous media with PHOTONICS. Nucl. Inst. Meth. A **581**, 619(2007). doi: 10.1016/j.nima.2007.07.143

[19] M. Ackermann, J. Ahrens, X. Bai et al., Optical properties of deep glacial ice at the South Pole. Journal of Geophysical Research Atmospheres. **111**, D13203(2006) doi: 10.1029/2005JD006687

[20] J. Nilsson, V. Cuplov, M. Isaksson, Identifying key surface parameters for optical photon transport in GEANT4/GATE simulations. Applied Radiation and Isotopes. **103**, 15(2015). doi: 10.1016/j.apradiso.2015.04.017

[21] R.S. Lu, A.K. Forrest, 3D surface topography from the specular lobe of scattered light. Optics and Lasers in Engineering. **45**, 1018(2007). doi: 10.1016/j.optlaseng.2007.04.008

[22] E. Hecht, in *Optics*, ed. by Addison-Wesley(Boston, 1974), pp. 71-80 and pp. 244-246

[23] A. Levin, C. Moisan, A more physical approach to model the surface treatment of scintillation counters and its implementation into DETECT. IEEE Nuclear Science Symposium. **2**, 702(1996) doi: 10.1109/NSSMIC.1996.591410

[24] E. Roncali, S.R. Cherry, Simulation of light transport in scintillators based on 3D characterization of crystal surfaces. Physics in medicine and biology. **58**, 2185(2013). doi: 10.1088/0031-9155/58/7/2185

[25] S. Riggi, P.L. Rocca, E. Leonora et al., GEANT4 simulation of plastic scintillator strips with embedded optical fibers for a prototype of tomographic system. Nucl. Inst. Meth. A **624**, 583(2010). doi: 10.1016/j.nima.2010.10.012

[26] H. Yi, Z. Zhang, Z.G. Xiao et al., Prototype studies on the forward MWDC tracking array of the external target experiment at HIRFL-CSR. Chinese Physics C **38**, 126002(2014). doi: 10.1088/1674-1137/38/12/126002

[27] A. Bellerive, J.R. Klein, A.B. McDonald et al., The Sudbury Neutrino Observatory. Nuclear Physics B **908**, 30(2016) doi: 10.1016/j.nuclphysb.2016.04.035

[28] B. Aharmim, Q.R. Ahmad, S.N. Ahmed et al., Determination of the ν_e and total ^8B solar neutrino fluxes using the Sudbury Neutrino Observatory Phase I data set. Phys. Rev. C **75**, 045505(2007). doi: 10.1103/PhysRevC.75.045502

[29] S. Fukuda, Y. Fukuda, T. Hayakawa et al., The Super-Kamiokande detector. Nucl. Inst. Meth. A **501**, 418(2003). doi: 10.1016/S0168-9002(03)00425-X

[30] J.P. Cravens, K. Abe, T. Iida et al., Solar neutrino measurements in Super-Kamiokande-II. Phys. Rev. D **78**, 032002 (2008). doi: 10.1103/PhysRevD.78.032002

[31] K. Abe, Y. Hayato, T. Iida et al., Solar neutrino results in Super-Kamiokande-III. Phys. Rev. D **83**, 052010(2011). doi: 10.1103/PhysRevD.83.052010

[32] T. Furuno, T. Kawabata, H.J. Ong et al., Performance test of the MAIKo active target. Nucl. Inst. Meth. A **908**, 215(2018). doi: 10.1016/j.nima.2018.08.042

[33] M Lindström, Track reconstruction in the ATLAS detector using elastic arms. Nucl. Inst. Meth. A **357**, 129(1995). doi: 10.1016/0168-9002(94)01544-9

[34] P.V.C. Hough, Machine Analysis of Bubble Chamber Pictures, Conf. Proc. C, 590914, 554(1959)

[35] M. Shiozawa, Reconstruction algorithms in the Super-Kamiokande large water Cherenkov detector. Nucl. Inst. Meth. A **433**, 240(1999). doi: 10.1016/S0168-9002(99)00359-9

[36] T.K. Gaisser, in *Cosmic Rays and Particle Physics*, ed. by Press Syndicates of the University of Cambrige(1990), pp.69-81